INTERNATIONAL JOURNAL FOR NUMERICAL METHODS IN FLUIDS
*Int. J. Numer. Meth. Fluids* 2007; **54**:103–118
Published online 28 November 2006 in Wiley InterScience (www.interscience.wiley.com). DOI: 10.1002/fld.1398

# A new method for direct simulations of flexible filament suspensions in non-zero Reynolds number flows

Dewei Qi*, †

*Paper Engineering, Chemical Engineering and Imaging, Wester Michigan University, Kalamazoo, MI 49008, U.S.A.*

SUMMARY

A new method for direct simulations of flexible filament suspensions in a non-zero Reynolds number flow is developed. For fluid domain, simulations are based on a lattice Boltzmann equation. For solid domain, a slender solid body is discretized into a chain of consecutive spherical segments contacting each other. A constraint force algorithm is proposed to warrant constant bonding distance between two neighbouring segments and non-slip velocity conditions at the contacting points so that the flexible filament moves and rotates as a whole body. The fibre could be bent and twisted in the model. Non-linear inertial interactions between fluid and flexible filament can be naturally studied by using this model embedded in the lattice Boltzmann scheme. The present flexible fibre method is tested by using a rigid particle method when the fibre stiffness is very large and by comparing the present results with theoretical and experimental results. It is demonstrated that the present results have a reasonable accuracy and that the computational results are consistent with the existed experimental results at non-zero Reynolds number flows. Copyright © 2006 John Wiley & Sons, Ltd.

Received 28 February 2006; Revised 28 September 2006; Accepted 3 October 2006

KEY WORDS: fibre suspensions; lattice Boltzmann equation; fibre orientation

## 1. INTRODUCTION AND BACKGROUND

Dynamics of flexible filaments in flows are important to understanding many phenomena encountered in biology, chemistry, physics and engineering. For example, bacteria uses flexible flagella

*Correspondence to: Dewei Qi, Paper Engineering, Chemical Engineering and Imaging, Wester Michigan University, Kalamazoo, MI 49008, U.S.A.
†E-mail: dewei.qi@wmich.edu

Contract/grant sponsor: Publishing Arts Research Council; contract/grant number: 98-1846389

to move. Flagella rotation will generate a flow field that affects flagella's swimming manner while eukaryotic flagella is used to propel sperm cells toward eggs. Another example is that fibre-like actin filaments are dynamic polymers whose ATP-driven assembly in the cell cytoplasm drives shape changes, cell locomotion and chemotactic migration. Recent visualization of F-actin, wormlike micelles and neurofilaments by using fluorescence microscopy reveal that these biopolymer chains exhibit a variety of conformational and dynamical behaviours depending on many factors, including polymer concentration, polymer stiffness, flow and mechanical stress [1].

In composite materials, the rheological property of the suspension may dominate forming process of injection molding of fibre-reinforced resin. The macroscopic properties of composite or suspensions such as elastic modulus and strength will depend on orientation of fibres. In the paper industry, distribution or structures of fibre suspensions at a high Reynolds number flow will determine drainage rate, screening, filtration and flocculation properties, in turn, production rate of paper because a fast drainage rate could lead to a higher machine speed.

Due to importance to science and engineering, many scientists reported their research results on flexible fibre suspension in both experiments and theories [2–5]. Forgacs and Mason [6] measured the rotation orbits of fibres when the flow is subjected to a shear in a diluted fibre suspension with a very low concentration. Interaction between fibres was neglected in such a low concentration. They observed 'springy', 'snake' and 'S-turn' rotations.

Several numerical methods are developed to simulate flexible filament motion and rheology properties. Yamamoto and Matsuoka [7, 8] proposed a method in which a slender fibre is approximated by a chain of spheres connected through a spring. The consecutive spheres are subjected to bending and torsion forces. Based on a zero-Reynolds number flow model where inertia was neglected, hydrodynamic forces were computed and fibre motion was simulated. Subsequently, Ross *et al.* [9] employed a chain of rigid spheroid connected through ball and socket joints to improve computation efficiency. In their model, the fibre length was fixed and not extensible. It seems that the fixed fibre length model is consistent with experiments. Later, Stokes and Green [10] used an immersed boundary method to consider the fibre influence on the fluid. The fibre was treated as massless. The simulations were carried out in a two-dimensional space. Further, following the Ross *et al*.'s work, Dong *et al*. [11] included wall effects in their simulation. Other different numerical simulations of fibre suspensions were reported by Tornberg *et al*. [12] and Fan *et al*. [13]. They employ a non-local slender body theory that yields an integral equation, along the filament centreline. All the mentioned works above were limited to zero Reynolds number flows where inertia of fluid and particles was ignored.

Currently, there is no any simulation method available to deal with flexible filaments in a finite Reynolds number flow. Therefore, a new method for simulation of flexible filament suspensions with inertia is urgently needed and will be developed. This new method is based on a lattice Boltzmann simulation scheme that is equivalent to solve the Navier–Stokes equations where nonlinear inertial effects are naturally included.

The developed method is employed to simulate motion of flexible rodlike particles under hydrodynamic forces. Dynamic information for both flexible fibres and fluid flows could be extracted from the numerical simulations. Section 2 will present simulation method including the lattice Boltzmann method and flexible fibre model as well as constraint force algorithm. Simulation results will be reported in Section 3. The final section makes some conclusions.



DOI: 10.1002/fld

## 2. SIMULATION METHOD

### 2.1. Flexible fibre model

Simulation domains can be divided into a solid region and a fluid region. In the solid region, a long filament is discretized and approximated by a chain of consecutive spheres similar to the work of Yamamoto and Matsuoka [7]. If the total number of spheres in a fibre is $N$ and the fibre length is $L$, the diameter of each sphere is $D = L/N = 2d$ or called bonding distance. If the consecutive spheres are labelled by an index $i$ in an increasing order, the each bonding direction can be defined by a unity vector

$$\mathbf{e}_i = \frac{\mathbf{R}_{i+1} - \mathbf{R}_i}{|\mathbf{R}_{i+1} - \mathbf{R}_i|} \tag{1}$$

where $\mathbf{R}_i$ is the position of the mass centre of the $i$th sphere.

The length of the fibre is a constant, i.e. extension or compression of the fibre is ignored in this model. However, the fibre can be bent and a bending angle $\theta_i$ can be measured through

$$\cos\theta_i = \mathbf{e}_i \circ \mathbf{e}_{i+1} \tag{2}$$

The bending moment is $\mathbf{M} = (EI/D)(\theta_i - \theta_{i0})\mathbf{b}$ where $\mathbf{b} = \mathbf{e}_i \times \mathbf{e}_{i-1}$ is the bending plane, $\theta_{i0}$ is the equilibrium bending angle. $EI$ is known as the bending rigidity with Young's modulus $E$ and the moment of inertia of the cross-section area $I = \frac{1}{4}\pi d^4$. Therefore, bending restore forces acting on sphere $i+1$, $i$ and $i-1$ can be calculated by

$$\mathbf{F}^{\mathrm{b}}_{i+1} = -\frac{1}{2D}\mathbf{M} \times \mathbf{e}_i \tag{3}$$

$$\mathbf{F}^{\mathrm{b}}_{i-1} = -\frac{1}{2D}\mathbf{M} \times \mathbf{e}_{i-1} \tag{4}$$

$$\mathbf{F}^{\mathrm{b}}_{i} = -(\mathbf{F}_{i+1} + \mathbf{F}_{i-1}) \tag{5}$$

A fibre may be subjected to a torsion torque and be twisted by an angle of $\phi$ around the bonding $\mathbf{e}_i$. Thus, a restoring torque will be

$$\mathbf{T}^{\mathrm{t}}_i = -k_{\mathrm{t}}(\phi_i - \phi_{i0})\mathbf{e}_i \tag{6}$$

where $k_{\mathrm{t}} = \pi d^3 G/4$, $G$ is the shear modulus, and $\phi_{i0}$ is the equilibrium twisting angle.

### 2.2. Lattice Boltzmann method

For the fluid region, the lattice Boltzmann method is applied to simulate the interactions between fluid and solid particles. The kinetic nature of lattice Boltzmann method enables it to simulate the complex geometry such as flexible web [14–21].

In lattice-Boltzmann (LB) method [15, 22–26], fluid particles reside on the lattice nodes and move to their nearest neighbours along the links with unit spacing in each unit time step. The lattice Boltzmann equation with Bhatnagar–Groos–Krook (BGK) [27] single relaxation time, is given by

$$f_\sigma(\mathbf{x} + \mathbf{e}_\sigma, t+1) = f_\sigma(\mathbf{x}, t) - \frac{1}{\tau}\left[f_\sigma(\mathbf{x}, t) - f^{\mathrm{eq}}_\sigma(\mathbf{x}, t)\right] \tag{7}$$



DOI: 10.1002/fld

where $f_\sigma(\mathbf{x}, t)$ is the fluid particle distribution function for particles with velocity $\mathbf{e}_\sigma$ at position $\mathbf{x}$ and time $t$, $f_\sigma^{\mathrm{eq}}(\mathbf{x}, t)$ is the equilibrium distribution function and $\tau$ is the single relaxation time.

The simulations will be performed using the D3Q15 model [22]. It possesses a rest particle state, six links with the nearest neighbours, and eight links with next nearest neighbours. Periodic boundary conditions in the flow direction with bounce back on the solid nodes will be used. $f_\sigma^{\mathrm{eq}}(\mathbf{x}, t)$ is taken as

$$f_\sigma^{\mathrm{eq}}(\mathbf{x}, t) = \omega_\sigma \rho_{\mathrm{f}} \{1 + 3(\mathbf{e}_\sigma \cdot \mathbf{u}) + \tfrac{9}{2}(\mathbf{e}_\sigma \cdot \mathbf{u})^2 - \tfrac{3}{2}(\mathbf{u} \cdot \mathbf{u})\} \tag{8}$$

where $\rho_{\mathrm{f}}$ is the density of the fluid, $\mathbf{u}$ is the velocity, $\sigma = 1$ represents the particles which move to the nearest neighbours, $\sigma = 2$ represents the particles which move to the next nearest neighbours, $\sigma = 0$ represents the particles which rest at the nodes. The weight coefficient $\omega_\sigma$ depends on the discrete velocity set $\mathbf{e}_\sigma$ and dimensions of space. In D3Q15 model, the discrete velocity set is

$$\mathbf{e}_\sigma = \begin{cases} (0, 0, 0), & \sigma = 0 \\ (\pm 1, 0, 0),\ (0, \pm 1, 0),\ (0, 0, \pm 1), & \sigma = 1 \\ (\pm 1, \pm 1, \pm 1), & \sigma = 2 \end{cases} \tag{9}$$

and the weight coefficient is

$$\omega_\sigma = \begin{cases} \frac{2}{9}, & \sigma = 0 \\ \frac{1}{9}, & \sigma = 1 \\ \frac{1}{72}, & \sigma = 2 \end{cases} \tag{10}$$

The mass density $\rho_{\mathrm{f}}$ and momentum density $\rho_{\mathrm{f}}\mathbf{u}$ are given by

$$\rho_{\mathrm{f}} = \sum_\sigma f_\sigma, \quad \rho_{\mathrm{f}}\mathbf{u} = \sum_\sigma f_\sigma \mathbf{e}_\sigma \tag{11}$$

In a widely used class of models, the kinematic viscosity $v$, is related to the relaxation time $\tau$ for convergence which is given by

$$v = \tfrac{1}{3}(\tau - \tfrac{1}{2}) \tag{12}$$

When any case of $R = 0$ is simulated, the terms of the second order of velocity in the fluid particle distribution function 8 is not included.

In order to match the fluid velocity with the solid boundary velocity at the fluid–solid interface, a moving boundary condition [28] is applied by

$$f_{\sigma'}(\mathbf{x}, t + 1) = f_\sigma(\mathbf{x}, t_+) - 6\omega_\sigma \rho_{\mathrm{f}} \mathbf{e}_\sigma \cdot \mathbf{U}_{\mathrm{b}} \tag{13}$$

where $\sigma'$ represents the reflecting direction and $\sigma$ denotes the incident direction of fluid particle at a node adjacent to the solid-surface with the boundary velocity $\mathbf{U}_{\mathrm{b}} = \mathbf{U}_0 + \boldsymbol{\Omega} \times \mathbf{x}_b$, $\mathbf{U}_0$ is the velocity of the mass centre of the corresponding solid particle, $\boldsymbol{\Omega}$ is its angular velocity, $\mathbf{x}_{\mathrm{b}} = \mathbf{x} + \frac{1}{2}\mathbf{e}_\sigma - \mathbf{R}$, $\mathbf{x}$ is the position of the node, $\mathbf{R}$ is the solid particle mass centre. The hydrodynamic force exerted on the solid particle at the boundary node is computed by

$$\mathbf{F}(\mathbf{x} + \tfrac{1}{2}\mathbf{e}_\sigma) = 2\mathbf{e}_\sigma (f_\sigma(\mathbf{x}, t_+) - 3\omega_\sigma \rho_{\mathrm{f}} \mathbf{U}_{\mathrm{b}} \cdot \mathbf{e}_\sigma) \tag{14}$$



DOI: 10.1002/fld

The total hydrodynamic force [15, 19] on the solid particle are produced, by

$$\mathbf{F}_i^{\mathrm{h}} = \sum \mathbf{F}(\mathbf{x} + \tfrac{1}{2}\mathbf{e}_\sigma) \pm \rho_{\mathrm{f}}(\mathbf{x}, t)\mathbf{u}(\mathbf{x}, t) \tag{15}$$

The summation is over all the boundary nodes on the fluid region associated with particle $i$. The second term on the right hand side of the equation above considers the local fluid momentum contribution whenever a fluid node either enters or leaves out of the solid region. The positive sign is used when the fluid node enters the solid region. The minus sign is used when the solid node becomes the fluid node and an equilibrium distribution function with the fluid velocity equal to the solid boundary velocity is added on the new fluid node. Thus, the total torques on the solid particle is

$$\mathbf{T}_i^{\mathrm{h}} = \sum (\mathbf{x} + \tfrac{1}{2}\mathbf{e}_\sigma - \mathbf{R}) \times (\mathbf{F}(\mathbf{x} + \tfrac{1}{2}\mathbf{e}_\sigma) \tag{16}$$

$$\pm \rho_{\mathrm{f}}(\mathbf{x}, t)\mathbf{u}(\mathbf{x}, t)) \tag{17}$$

In order to prevent spheres or fibre from overlap, a short range repulsive force $\mathbf{F}_j^{\mathrm{r}}$ on sphere $i$ by sphere $j$ is added [9]

$$\begin{aligned} \mathbf{F}_i^{\mathrm{r}} &= K \exp\left[-H\frac{R_{ij} - D}{D}\right]\mathbf{e}_{ij} \quad \text{if } R_{ij} \geqslant D \\ &= K\,\mathbf{e}_{ij} \qquad\qquad\qquad\qquad\quad \text{if } R_{ij} < D \end{aligned} \tag{18}$$

where $H$ controls the repulsive force range and $K$ controls the force strength. We use $K = 1$ and $H = 10$, thus the force range is $\frac{1}{10}$.

### 2.3. Constraint forces

The equations of translational and rotational motion for each constituent sphere of the fibre may be expressed as

$$m\dot{\mathbf{U}}_i = \mathbf{F}_i \tag{19}$$

$$I\dot{\boldsymbol{\Omega}}_i = \mathbf{T}_i \tag{20}$$

where

$$\mathbf{F}_i = \mathbf{F}_i^{\mathrm{b}} + \mathbf{F}_i^{\mathrm{h}} + \mathbf{F}_i^{\mathrm{r}} \tag{21}$$

$$\mathbf{T}_i = \mathbf{T}_i^{\mathrm{t}} + \mathbf{T}_i^{\mathrm{h}} \tag{22}$$

When we integrate the Newtonian dynamic equations above, it is important that a constraint algorithm should be developed to force the chain of the discretized spheres moving and rotating as a whole body.

Therefore, two restraint forces and corresponding torques (if any) have to be added to the equations above for each sphere. The first force $G_i\mathbf{e}_i$, called radial constraint force, is used to keep the bonding distance constant. It is obvious that this force should be in the direction along the bonding vector connecting the mass centres of two spheres as shown in Figure 1.

The second force $\mathbf{Q}_i$, called tangential constraint force (see Figure 1), is used to maintain a non-slip velocity boundary condition at contacting points of the two neighbouring spheres so that



DOI: 10.1002/fld

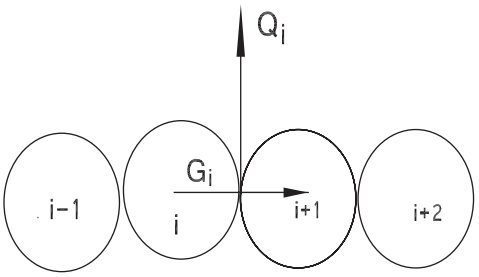


Figure 1. Illustration of radial and tangential constraint forces, $G_i\mathbf{e}_i$ and $\mathbf{Q}_i$, at the contacting point.

each sphere independently rotating about its own mass centre is removed. Its direction should be perpendicular to the bonding vector at the contacting points. Essentially, this is a rotational restraint force. It is obvious that $G_i\mathbf{e}_i$ and $\mathbf{Q}_i$ are nothing but the components of the constraint force acting on particle $i$. $G_i\mathbf{e}_i$ is the component parallel to the $\mathbf{e}_i$, while $\mathbf{Q}_i$ is the component perpendicular to the $\mathbf{e}_i$.

Further, to satisfy the two conditions at every time step, a leap-frog algorithm [29–31], for integration of motion equations is modified. For radial distance constraint, the position of sphere can be written as

$$\mathbf{R}_i(t+h) = \mathbf{R}'_i(t+h) + \frac{h^2}{m}(G_i\mathbf{e}_i - G_{i-1}\mathbf{e}_{i-1}) \tag{23}$$

$$\mathbf{R}_{i+1}(t+h) = \mathbf{R}'_{i+1}(t+h) + \frac{h^2}{m}(G_{i+1}\mathbf{e}_{i+1} - G_i\mathbf{e}_i) \tag{24}$$

where $\mathbf{R}'_i(t+h)$ and $\mathbf{R}'_{i+1}(t+h)$ are the positions without constraint forces, $h$ is the length of time step, $G_i\mathbf{e}_i$ is the radial constraint force on sphere $i$ by sphere $i+1$. In the half leap-frog algorithm

$$\mathbf{R}'_i(t+h) = \mathbf{R}_i(t) + h\mathbf{U}_i(t+\tfrac{1}{2}h) \tag{25}$$

where

$$\mathbf{U}_i\left(t+\frac{1}{2}h\right) = \mathbf{U}_i\left(t-\frac{1}{2}h\right) + \frac{h}{m}\mathbf{F}_i(t) \tag{26}$$

here $\mathbf{F}_i$ is the force and $\mathbf{U}_i$ is the velocity of the mass centre of particle $i$.

To keep the constant bonding distance we have

$$(\mathbf{R}_{i+1}(t+h) - \mathbf{R}_i(t+h))^2 = D^2 \tag{27}$$

Substituting Equations (23) and (24) into the equation above we obtain

$$A_1 G = C_1 \tag{28}$$

where $A_1$ is a matrix of $N-1$ by $N-1$, the constraint force matrix $G$ and $C_1$ are $N-1$-dimensional vector.

For the rotational constraint, the velocity at the contacting point between spheres $i$ and $i+1$ could be written as

$$\mathbf{V}_i(t+h) = \mathbf{U}_i(t+h) + \mathbf{\Omega}_i(t+h) \times d\mathbf{e}_i \tag{29}$$



DOI: 10.1002/fld

and

$$\mathbf{V}_{i+1}(t+h) = \mathbf{U}_{i+1}(t+h) - \boldsymbol{\Omega}_{i+1}(t+h) \times d\mathbf{e}_i \tag{30}$$

where

$$\mathbf{U}_i(t+h) = \mathbf{U}'_i(t+h) + \frac{3h}{2m}(\mathbf{Q}_i - \mathbf{Q}_{i-1}) \tag{31}$$

$$\mathbf{U}_{i+1}(t+h) = \mathbf{U}'_{i+1}(t+h) + \frac{3h}{2m}(\mathbf{Q}_{i+1} - \mathbf{Q}_i) \tag{32}$$

$$\boldsymbol{\Omega}_i(t+h) = \boldsymbol{\Omega}'_i(t+h) \tag{33}$$

$$+ \frac{3h}{2I}(d\mathbf{e}_i \times \mathbf{Q}_i + d\mathbf{e}_{i-1} \times \mathbf{Q}_{i-1}) \tag{34}$$

$$\boldsymbol{\Omega}_{i+1}(t+h) = \boldsymbol{\Omega}'_{i+1}(t+h) \tag{35}$$

$$+ \frac{3h}{2I}(d\mathbf{e}_{i+1} \times \mathbf{Q}_{i+1} + d\mathbf{e}_i \times \mathbf{Q}_i) \tag{36}$$

where $\mathbf{U}'_i$ and $\boldsymbol{\Omega}'_i$ are velocity and angular velocity without the restraint forces and can be written as

$$\mathbf{U}'_i(t+h) = \mathbf{U}_i\left(t - \frac{1}{2}h\right) \tag{37}$$

$$+ \frac{3h}{2m}(\mathbf{F}_i(t) + G_i\mathbf{e}_i - G_{i-1}\mathbf{e}_{i-1}) \tag{38}$$

$$\boldsymbol{\Omega}'_i(t+h) = \boldsymbol{\Omega}_i\left(t - \frac{1}{2}h\right) + \frac{3h}{2I}\mathbf{T}_i(t) \tag{39}$$

To satisfy the non-slip velocity at the contacting points, we set $\mathbf{V}_i(t+h) = \mathbf{V}_{i+1}(t+h)$ for $i = 1, \ldots, N-1$ and obtain

$$A_2 Q = C_2 \tag{40}$$

where $A_2$ is a matrix of $3(N-1)$ by $3(N-1)$, the tangential constraint force matrix $Q$ and $C_2$ are a $3(N-1)$-dimensional vectors. Equations (28) and (40) can be solved by using a singular decomposition method [31].

## 3. RESULTS AND DISCUSSIONS

### *3.1. Zero Reynolds numbers*

Motion of a single flexible fibre in a Couette flow is simulated. The fibre density is equal to the fluid density in this work. The single fibre is discretized as a chain of spheres, each with a diameter



DOI: 10.1002/fld

of 8. The fibre with an aspect ratio of $r = 9$ is moved and rotated between the bounded and sheared walls. The total fibre length is 72. The confinement ratio of the channel width to the fibre length is 1.5 for all the present simulations. The shear gradient is added in the $x$-direction, the vorticity vector direction is in the $z$-direction, and the flow is in the $y$-direction.

For the very stiff fibre with $E = 3.75$, its rotational behaviour looks like a rigid fibre. To examine the rotation, an angular distribution function is defined as the probability of the angle $\phi$ of the fibre principal axis with the flow or $y$-direction per unit angle. The simulation results of angular distribution function for the fibre at the Reynolds number $R = 0$ are plotted in Figure 2 and compared with the theoretical results of Jeffery formula [32] for ellipsoid

$$\phi = a\tan\left[r_e \tan\left(\lambda t \frac{r_e}{r_e^2 + 1}\right)\right] \tag{41}$$

where $\phi$ is the angle of the fibre with the horizontal direction (the $y$- or flow direction), $\lambda$ is the shear rate and $t$ is the time. Since the cylindrical shape is different from ellipsoid, equivalent fibre aspect ratio is used to take into account the difference. Cox [33] employed theoretical analysis and comparison with experiments to obtain equivalent aspect ratio of cylinder

$$r_e = 1.24 \frac{r}{\sqrt{\ln r}} \tag{42}$$

The equation reproduced well experimental data. However, the shape of a chain of spheres is different from either cylinder or ellipsoid. Therefore, equivalent aspect ratio for the present fibre model should be slightly different from both of them. We calculate the equivalent aspect

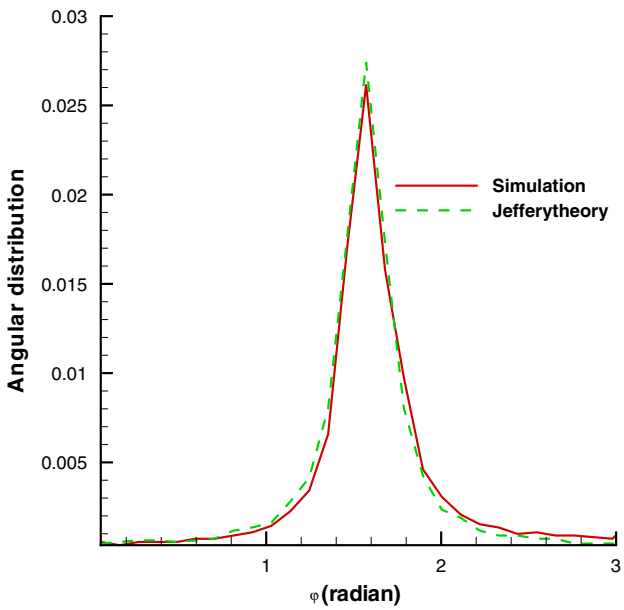


Figure 2. The simulation result of angular distribution function is compared with Jeffery theory. The equivalent aspect ratio of the fibre is $r_e = 7.8$.



DOI: 10.1002/fld

ratio $r_e = 7.8$ for the fibre using formula $t\lambda = 2\pi(r_e + 1/r_e)$. The period $t\lambda$ comes from the result of a simulation at $R = 0$. We make a caution here. The formula is for the simple shear flow without wall effect. The wall effect may increase the period slightly. It is not surprised that the calculated equivalent aspect ratio $r_e = 7.8$ is slightly larger than the value of 7.5 predicted by using Equation (42) due to the shape difference between the current fibre model and cylinder.

It is clear that the simulation result is in fairly good agreement with the theoretical result in Figure 2 although a small deviation from Jeffery's theory exists due to the wall effect. We have also simulated several cases where fibres have different flexibilities. In simulations $E$ is varied to obtain different flexibilities while keeping all the other conditions same. We observe that as flexibility increases the rotation patterns are changed from one pattern to other pattern.

As stiffness is reduced from a rigid fibre, it starts to be bent like a leaf-spring when it approaches an angle of 45° with the horizontal direction and then flicks straight as its long body rotates close to the horizontal or $y$ direction as shown in the first row $E = 1.25$ of Figure 3. This rotating orbital is called 'springy' [6]. When the fibre flexibility increases (where $E = 0.25$), fibre deformation becomes more pronounced as shown in the second row. As $E = 0.1$, the more flexible fibre has 'snake' and 'S-turns' when its long body is mainly in the cross fluid or $x$ direction the fibre is stretched again when its long body is along the flow or $y$ direction as shown in the 3rd and 4th rows of Figure 3. As the fibre flexibility continuously increases or $E = 0.025$, 'complex' rotations appear. In the pattern, the curved body remains all the time, the fibre is never stretched (the last

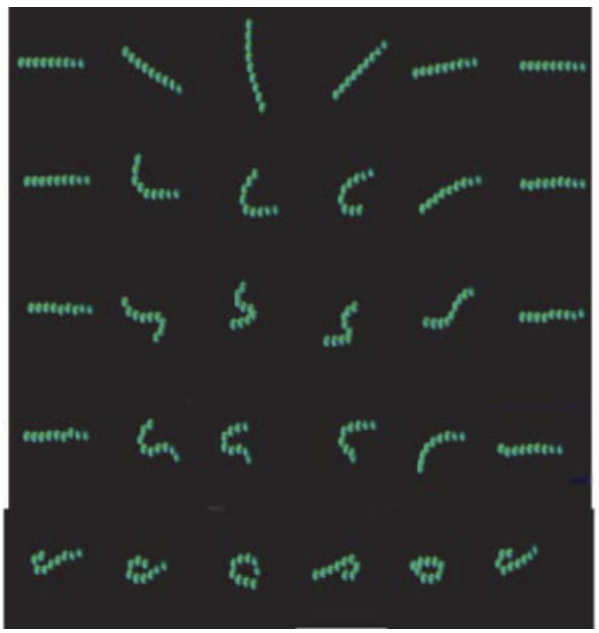

Figure 3. The snapshots at different times for fibres with $E = 1.25$ (the 1st row), $E = 0.25$ (2nd row), $E = 0.1$ (the 3rd and 4th rows) $E = 0.025$ (5th row) during a half periodic time (all other simulation conditions are the same). The fibre aspect ratio is $r = 9$. The time is in an increasing order from the left to the right in the same row.



DOI: 10.1002/fld

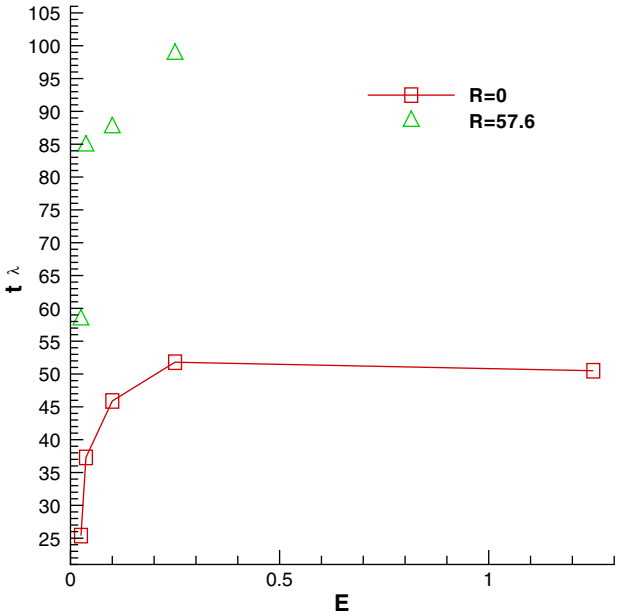


Figure 4. The period decreases as flexibility increases and the period increases as the Reynolds number increase due to inertia.

row in Figure 3). These rotation patterns in Figure 3 obtained from our simulations are consistent with experimental observation.

If we plot the displacements of the end spheres of a fibre as a function of time, then the rotational period can be measured from the variation of the displacement. We demonstrate that the period of rotation of fibre in the Couette flow at $R = 0$ decreases as flexibility increases in Figure 4 (square signs) and the basic trend is the same as that in experiments [6].

### 3.2. *Non-zero Reynolds numbers*

In order to further verify the validation of the present method at non-zero Reynolds number flows, we run a pair of simulations at the same conditions but using two different methods and compare their results. A rigid fibre consisting of five spheres side by side is simulated by using the rigid particle method reported in References [15, 18]. The rigid particle method has been extensively tested and is used to test the present flexible fibre method. A flexible fibre containing the same number and size of spheres is simulated by using present method. This fibre has a very large stiffness of $E = 37.5$ and it may, therefore, be considered as a rigid fibre. For these tests, two different simulation box sizes are used to check the size effects. One box size is $60 \times 84 \times 84$, the fibre length is 40 and diameter of each sphere is 8. Other box size is $90 \times 126 \times 126$ and the corresponding fibre length and diameter are 60 and 12. The results have no significant difference for the two different size simulation boxs. At the final stages of simulations the results of the displacements of sphere A at one end of the fibre and sphere B at other end as a function of time ($t\lambda$) by using both the methods are plotted in Figure 5(a) for $x$-components and (b) for $y$-components at $R = 16.0$ and in Figure 6 for those at $R = 26.67$. The fibre rotates in the $xy$-plane



DOI: 10.1002/fld

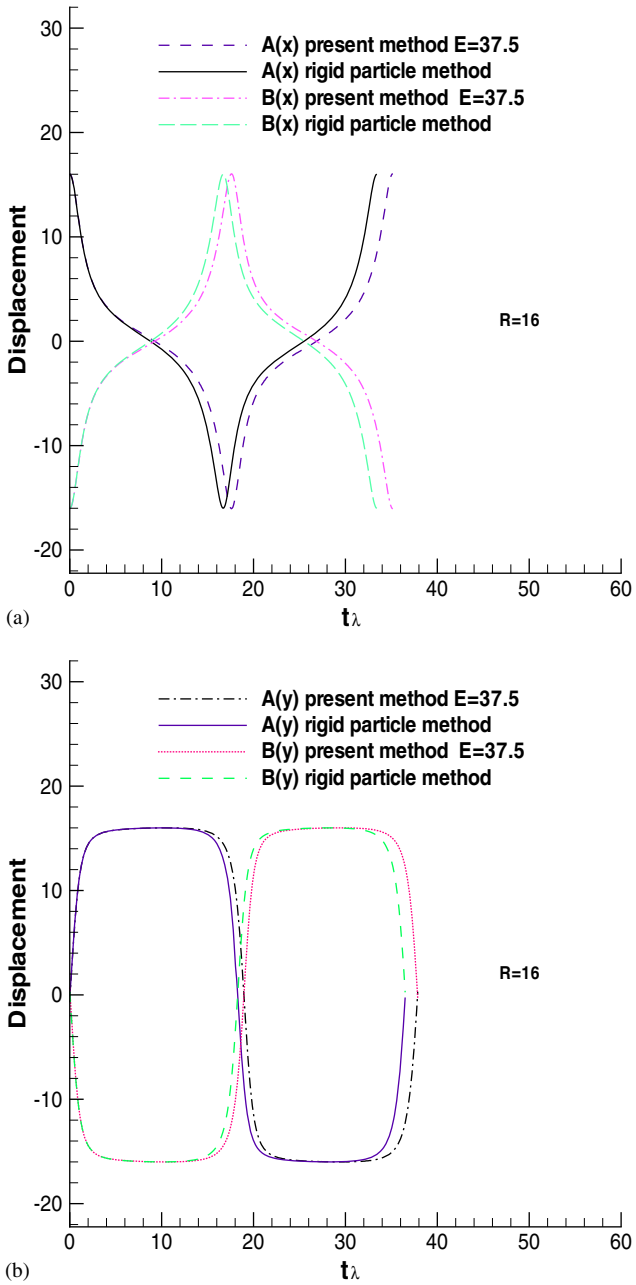


Figure 5. The displacements as a function of time by using rigid particle method and by using present flexible fibre method. A($X$) and A($Y$) are the $x$- and $y$-components of the displacements for end sphere A in a fibre, B($X$) and B($Y$) are those for other end sphere B. The displacements in the figure is due to rotation about the mass centre of the centre sphere in a fibre at $R = 16$: (a) for the $x$-components; and (b) for $y$-components.



DOI: 10.1002/fld

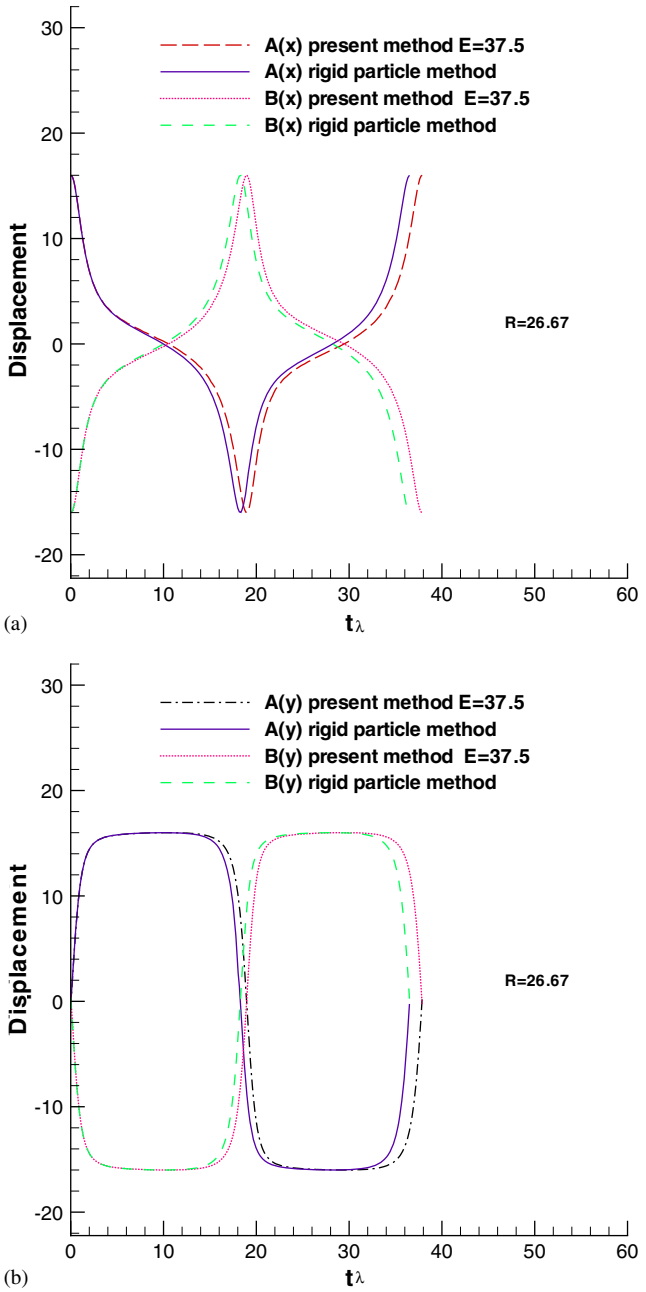


Figure 6. The same as the Figure 5 except $R = 26.67$.



DOI: 10.1002/fld

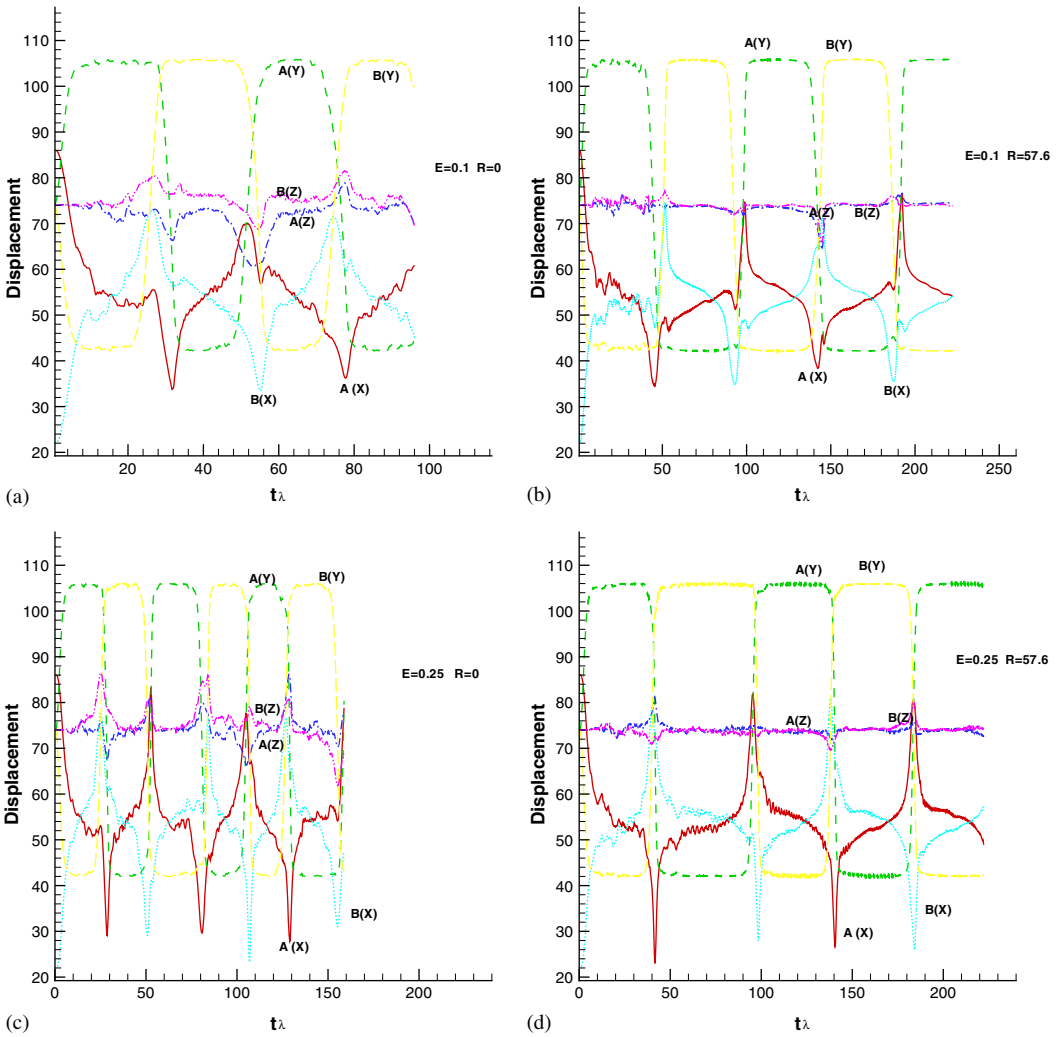


Figure 7. The displacements for end spheres A and B due to rotation are shown for the fibre with $E = 0.1$ at: (a) $R = 0$; and (b) $R = 57.6$ and for the fibre with $E = 0.25$ at: (c) $R = 0$; and (d) $R = 57.6$. A($x$), A($y$) and A($z$) are the displacements in $x$-, $y$- and $z$-components for end sphere A. B($x$), B($y$), and B($z$) are those for end sphere B.

perpendicular to the vorticity or $z$-direction. The displacements in the $z$-direction do not change much and need not be shown. Although the curves in Figures 6 and 7 by using the rigid particle method are not overlapped with those by using the present method, they are very close to each other. For the case of $R = 16$, the result of period $p = 35.16$ by using the present method is only 5% larger than that of period $p = 33.5$ by using rigid particle method as shown in Figure 5. For the case of $R = 26.67$, the period difference is within 4% as shown in Figure 6. The small difference between two methods validates the flexible fibre method within a reasonable accuracy.



DOI: 10.1002/fld

To show inertial effects, several simulations are further performed for the flexible fibres with the aspect ratio of $r = 9$ in a shearing flow channel at different Reynolds numbers. It is noted that a flexible fibre will be bent during rotating. Therefore its largest dimension or length during rotation varies, depending on the fibre flexibility and shear rates of flows. In this work, for comparison purpose, we simply use the fibre dimension or length when the fibre is rigid to define Reynolds number $R = \lambda L^2/v$. However, the actual Reynolds number of the fibre should be determined by the largest length of the fibre dimension during rotation and be generally lower than that calculated by using the definition. The displacements of fibre end sphere A and B are shown in Figure 7(a) and (b) for the fibre with $E = 0.1$ at $R = 0$ and 57.6 and in Figure 7(c) and (d) for the fibre with $E = 0.25$ at the same Reynolds numbers. The translation of the mass centre of the centre sphere of the fibre is hidden to exhibit displacements due to rotation only. It appears that the period is much larger for the case of $R = 57.6$ than the case of $R = 0$ at the same fibre stiffness. Figure 8 presents more evidence that the period increases as the Reynolds number increases for the fibre of $E = 0.1$. The same inertial effect has been investigated and reported [34, 35] for rigid circular and elliptical particles. Kossack and Acrivos predicted that as the Reynolds number increases the rotational period of a cylinder increases. Ding *et al.* [36] reported the similar numerical results for elliptical and ellipsoidal particles in shearing flows. Zettner and Yoda [37] experimentally confirmed the previous authors' findings. It seems that the inertia significantly slows down the rotation of the flexible fibre due to a negative torque generated by a recirculating flow around the fibre in the central region. The present results are consistent with the previous findings.

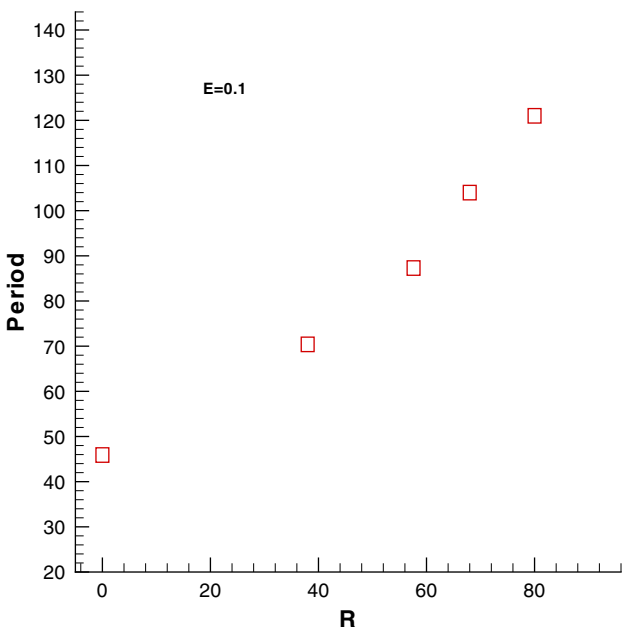


Figure 8. The period as a function of Reynolds numbers for the flexible fibre with $E = 0.1$.



DOI: 10.1002/fld

## 4. CONCLUSIONS

A new method for simulations of flexible fibres is developed. In the method, the fibre is discretized as a chain of contacting spheres. Two constraint forces are proposed to enforce non-slip velocity boundary condition and constant bonding distance at the contacting points. Subsequently constraint algorithms are developed to ensure the boundary conditions to be satisfied at every time step. Using this method, the simulations reproduce rotational patterns, such as 'springy', 'snake', 'S' and 'complex' orbits. The results also show that rotational period decreases as fibre flexibility increases. At non-zero Reynolds number, the rigid particle method is used to test the present flexible fibre method. The result by using the present method is in fairly good agreement with that by using the rigid particle method when fibre is very stiff. As the Reynolds number in the tested range increases, the period increases. The results are consistent with experimental results. It is demonstrated that the newly developed method is valid and faithful to physics of flexible fibre suspensions in a non-zero Reynolds number flow.

ACKNOWLEDGEMENTS

A valuable discussion with Professor Qiji Zhu, at the Mathematical Department of Western Michigan University, is greatly appreciated. He brings my attention to a singular decomposition method in solving constraint forces. My appreciations are also going to Miss Xiaoying Rong who drew some graphs. Finally, this work is partially supported by the Forest Product Laboratories of USDA.

REFERENCES

1. Dogic Z, Zhang J, Lau AWC, Aranda-Espinoza H, Dalhaimer P, Discher DE, Kamien RD, Janmey PA, Lubensky TC, Yodh AG. Elongation and fluctuations of semiflexible polymers in a nematic solvent. *Physical Review Letters* 2004; **92**:125503.
2. Leal LG. The low motion in a viscous fluid. *Journal of Fluid Mechanics* 1975; **69**:305.
3. Leal LG. Particle motion in a viscous fluid. *Annual Review of Fluid Mechanics* 1980; **271**:311.
4. Doyle PS, Shaqfeh ESG, Gast AP. Dynamic simulation of freely draining flexible polymers in steady linear flows. *Journal of Fluid Mechanics* 1997; **334**:251–291.
5. Jendrejack RM, Schwartz DC, de Pablo JJ, Graham MD. Shear-induced migration in flowing polymer solutions: simulation of long-chain dna in microchannels. *Journal of Chemical Physics* 2004; **120**:2513.
6. Forgacs L, Mason SG. Particle motion in sheared suspension. *Journal of Colloid Science* 1959; **14**:473–491.
7. Yamamoto S, Matsuoka T. A method for dynamics simulation of rigid and flexible fibres in a flow field. *Journal of Chemical Physics* 1992; **98**:644–650.
8. Ymamoto S, Matsuoka T. Viscosity of dilute suspensions of rodlike particles: a numerical simulation method. *Journal of Chemical Physics* 1994; **100**:3317–3324.
9. Ross R, Klingenberg D. Dynamics simulation of flexible fibers composed of linked rigid bodies. *Journal of Chemical Physics* 1997; **106**:2949–2960.
10. Stokie JM, Green SI. Simulating the motion of flexible pulp finer using the immersed boundary method. *Journal of Computational Physics* 1998; **147**:147–165.
11. Dong S, Feng X, Salcudean M, Gartshore I. Concentration of pulp fibers in 3d turbulent channel flow. *Journal of Multiphase Flow* 2003; **29**:1–21.
12. Tornberg AK, Shelley MJ. Simulating the dynamics and interactions of flexible fibers in Stokes flows. *Journal of Computational Physics* 1998; **147**:147.
13. Fan X, Phan-Thien N, Zheng R. A direct simulation of fiber suspensions. *Journal of Non-Newtonian Fluid Mechanics* 1998; **74**:113.
14. Koch DL, Ladd AJC. Moderate Reynolds number flows through periodic and random arrays of aligned cylinders. *Journal of Fluid Mechanics* 2001; **349**:31.



DOI: 10.1002/fld

15. Qi D. Simulations of fluidization of cylindrical particles in a 3-d space. *Journal of Multiphase Flow* 2000; **27**:107.
16. Qi D. Lattice Boltzmann simulations on fluidization of rectangular particles. *Journal of Multiphase Flow* 2000; **26**:421.
17. Zhang J, Fan LS, Zhu C, Pfeffer R, Qi D. Dynamic behavior of collision of elastic spheres in viscous fluids. *Journal of Powder Technology* 1999; **106**:98.
18. Qi D. Lattice Boltzmann simulations of particles in non-zero Reynolds number flows. *Journal of Fluid Mechanics* 1999; **385**:41.
19. Aidun CK, Lu Y, Ding E. Direct analysis of particulate suspensions with inertia using the discrete Boltzmann equation. *Journal of Fluid Mechanics* 1998; **373**:287.
20. Feng Z, Michaelides E. The immersed boundary-lattice Boltzmann method for solving fluid-particles interaction problems. *Journal of Computational Physics* 2004; **195**:602.
21. Feng Z, Michaelides E. Proteus: a direct forcing method in the simulations of particulate flows. *Journal of Computational Physics* 2005; **202**:20.
22. Qian Y, d'Humieres D, Lallemand P. Lattice BGK models for Navier–Stokes equation. *Europhysics Letters* 1992; **17**:479.
23. Chen S, Doolen GD. Lattice Boltzmann method for fluid flows. *Annual Review of Fluid Mechanics* 1998; **30**:329.
24. Chen H, Chen S, Matthaeus WH. Lattice Boltzmann method for fluid flows. *Physical Review A* 1992; **45**:R5339.
25. Gunstensen AK, Rothman DH. A Galilean-invariant immiscible lattic gas. *Physica D* 1991; **47**:53.
26. McNamara G, Zanetti G. Use of the Boltzmann equation to simulate lattice-gas automata. *Physical Review Letters* 1988; **61**:2332.
27. Bhatnagar PL, Groos EP, Krook M. *Physical Review* 1954; **94**:511–525.
28. Ladd AJC. Numerical simulations of particle suspensions via a discretised Boltzmann equation. Part 1. Theoretical foundation. *Journal of Fluid Mechanics* 1994; **271**:285.
29. Allen MP, Tildesley DJ. *Computer Simulation of Liquids*. Oxford University Press: Oxford, 1989.
30. Ryckaert J, Ciccott G, Berendson HJC. Integration of the cartesian equations of motion of a system with constraints: molecular dynamics of *n*-alkanes. *Journal of Computational Physics* 1977; **23**:327.
31. Press WH, Teukolsky SA, Vetterling WT, Flannery BP. *Numerical Recipes in Fortran the Art of Scientific Computing*. Cambridge University Press: Cambridge, MA, 1992.
32. Jeffrey GB. The motion of ellipsoidal particles immersed in a viscous fluid. *Proceedings of the Royal Society of London*, *Series A* 1922; **102**:161.
33. Cox RG. The motion of long slender bodies in a viscous fluid, part 2 shear flow. *Journal of Fluid Mechanics* 1971; **45**:625.
34. Kossack CA, Acrivos A. Steady simple flow past a circular cylinder at moderate Reynolds numbers: a numerical solution. *Journal of Fluid Mechanics* 1974; **66**:343.
35. Poe GG, Acrivos A. Closed-streamline flows past rotating single cylinders and spheres: inertia effect. *Journal of Fluid Mechanics* 1975; **72**:605.
36. Ding E, Aidun CK. The dynamics and scaling law for particles suspended in shear flow with inertia. *Journal of Fluid Mechanics* 2000; **423**:317.
37. Zettner CM, Yoda M. Moderate-aspect-ratio elliptical cylinders in simple shear with inertia. *Journal of Fluid Mechanics* 2001; **442**:241.



DOI: 10.1002/fld